Volume 17 Number 15 7 August 2017 Pages 2531–2684

Lab on a Chip

Devices and applications at the micro- and nanoscale

rsc.li/loc

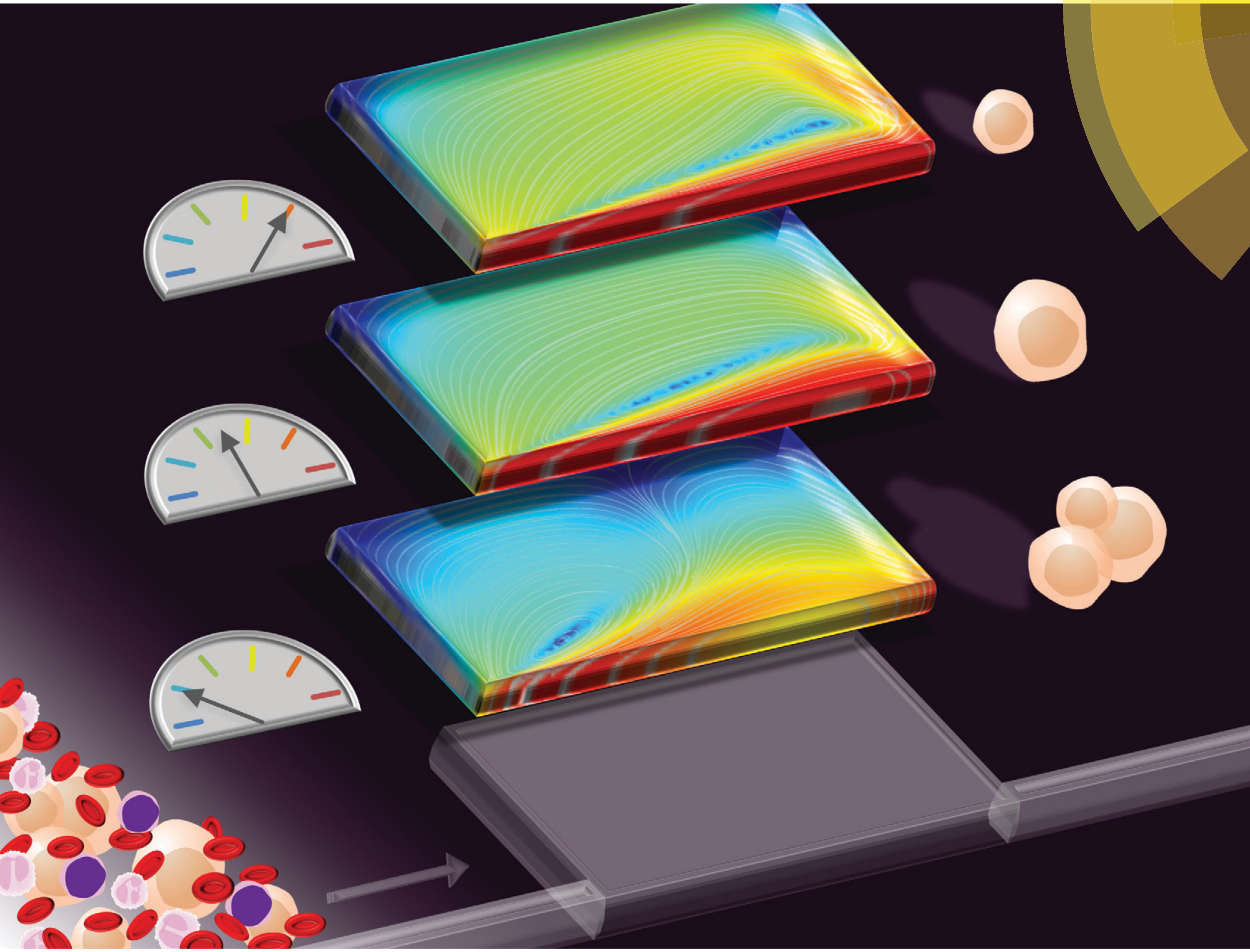

ISSN 1473-0197

ROYAL SOCIETY OF CHEMISTRY

PAPER
Dino Di Carlo *et al.*
Size-tunable microvortex capture of rare cells

Lab on a Chip

PAPER

View Article Online
View Journal | View Issue

Check for updates

Cite this: *Lab Chip*, 2017, **17**, 2542

Size-tunable microvortex capture of rare cells†

Reem Khojah, Ryan Stoutamore and Dino Di Carlo *

Received 31st March 2017,
Accepted 30th May 2017

DOI: 10.1039/c7lc00355b

rsc.li/loc

Inertial separation of particles and cells based on their size has advanced significantly over the last decade. However, size-based inertial separation methods require precise tuning of microfluidic device geometries to adjust the separation size of particles or cells. Here, we show a passive capture method that targets a wide size range of cells by controlling the flow conditions in a single device geometry. This multimodal capture device is designed to generate laminar vortices in lateral cavities that branch from long rectangular channels. Micro-vortices generated at lower Reynolds numbers capture and stabilize large particles in equilibrium orbits or limit cycles near the vortex core. Other smaller particles or cells orbit near the vortex boundaries and they are susceptible to exiting the cavity flow. In the same cavity, however, at higher Reynolds number, we observe small particles migrating inward. This evolution in limit cycle trajectories led to a corresponding evolution in the average size of captured particles, indicating that the outermost orbits are less stable. We identify three phases of capture as a function of Reynolds number that give rise to unique particle orbit trajectories. Flow-based switching overcomes a major engineering challenge to automate capture and release of polydisperse cell subpopulations. The approach can expand clinical applications of label free trapping in isolating and processing a larger subset of rare cells like circulating tumor cells (CTCs) from blood and other body fluids.

1 Introduction

Microfluidic systems have proven to be efficient and tunable platforms for general micro-scale manipulation and analysis of rare cells.[1] Many technologies separate cells by either inducing external forces (active separation), or using intrinsic hydrodynamic forces (passive separation).[2] Active technologies were developed for cell separation such as dielectrophoresis (DEP),[3–5] magnetophoresis (MP),[6–9] acoustophoresis (AP)[10–14] and optical tweezers.[15,16] They allow precise and tunable control of target particle motion in suspension. However, external forces have to be balanced with limited flow speeds, resulting in a significant throughput penalty.

Passive technologies, on the other hand, are simple, robust and solely based on controlling hydrodynamic properties of the flow.[17] Methods such as pinched flow fractionation (PFF),[18–20] deterministic lateral displacement (DLD),[21] microfiltration[22,23] and inertial microfluidics[24–27] were used for continuous cell separation. Inertial microfluidics, in particular, enables high-throughput technologies to process large sample volumes in a short analysis time.[28] These features are favorable for blood component isolation and processing.[29]

In an inertia-dominated regime, particle motion does not simply follow fluid streamlines.[30] In the case of inertial flow in a rectangular channel, the physical properties of suspended particles influence their motion through inertial migration or inducing secondary flows.[31,32] This enables precise manipulation (*i.e.* focusing, sorting and separation) of bio-particles by controlling inertial flow properties.[33] However, without changing the device geometry it is challenging to modulate size-based separation and capture of rare cells with a distribution of sizes and deformability.[34]

Recently, our group developed high-throughput cell entrapment technology that concentrates cells into a small volume in microvortices.[35] This enables cell processing (staining,[36] conjugation,[37] transfection[38] and deformability testing[39]) in the same device. The system can isolate circulating tumor cells (CTCs) from patient samples with high purity and efficiency,[40–42] but lacks the ability to adjust the capture size cut-off in a single device. This is a main limitation, since cells from the same or a different lineage can be polydisperse in size.

In this work, we uncover a new size-dependent particle trapping phenomenon in microvortices that enables tunable size-based cell capture. There has been broad interest in size-based particle separation in vortical flows formed in T-junctions,[43] tubular sudden expansions[44,45] and confined cavity flows.[37,46,47] Particles enter orbits in these cavity flows with a radial distance that depends on particle size. We explored the evolution of size-dependent radial orbits as a function of Reynolds number in a single cavity (Fig. 1A). Through modulating the balance of intrinsic inertial and viscous forces, we

---

Department of BioengineeringUniversity of California, Los Angeles, CA, 90055, USA. E-mail: dicarlo@seas.ucla.edu

† Electronic supplementary information (ESI) available. See DOI: 10.1039/c7lc00355b

characterize three inertial phases that influence size-based particle entrapment in microvortex flows (Fig. 1B). Each flow condition generates a limit cycle or stable orbits for a certain particle size. We provide a new systemic understanding of the three selective trapping phases based on the cavity's vortical flow properties. We take advantage of this new understanding to perform cell separation across a range of conditions optimized to enrich different sizes. Flow-induced switching enables isolation and capture of an expanded size range of cells in a single device geometry. This facilitates total analysis systems for bio-fluid processing for many diagnostic applications and downstream analyses.

2 Methods

2.1 Device fabrication

A straight rectangular channel (H_{ch} = 70 μm, W_{ch} = μm, L_{ch} = 3 cm) was formed from a master mold fabricated *via* standard soft photolithography. KMPR 1050 (Microchem) photoresist was used for this process. Trapping reservoirs were placed 1 cm away from the inlet to the rectangular channel. All cavities with different aspect ratios (AR = 1, 2 and 3) were made of the same height (H = 70 μm) (Fig. S1†). A PDMS elastomer and a curing agent (Sylgard 184, Dow Corning, Midland, MI) were mixed at a ratio of 10:1 and the mixture was poured onto the master mold and degassed for 60 minutes to remove all trapped bubbles. The master mold was placed in a 68 °C oven for 24 hours to thoroughly cure the PDMS. The cured PDMS replica was peeled away from the master mold. Inlet and outlet holes were punched in the PDMS replica which was irreversibly bonded to a glass slide by exposing both PDMS and glass surfaces to O_2 plasma for 37 s, at 500 mTorr and an 80 W power (Harrick Plasma, Ithaca, NY).

2.2 Device operation

Particle suspensions were pumped into the device using a syringe pump (Harvard Apparatus, Holliston, MA, USA) through polyetheretherketone (PEEK) tubing (Upchurch Scientific). The device was primed with PBS buffer for 1 min to form the vortex topology at different flow rates ranging from 100–1000 μL min^{-1}. Fluid was collected at the end of the chip in a new capped syringe for reruns. To avoid particle sedimentation, syringes with suspensions were mixed and changed in each run to maintain a uniform distribution of particles. The flow rate of a single channel device was multiplied by the number of parallel channels in the high-throughput Vortex HT device described in previous studies.[39,42,48] The number of cells passing through the cavity were normalized across different flow rates to obtain 1000 cells to pass through a single cavity for size selectivity studies and 350 cells in the Vortex HT device for capturing efficiency studies (Note S1†).

2.3 Image analysis

The cavity was viewed using a microscope (Nikon Ti-U) illuminated by a mercury arc lamp with a 10× objective of an effective pixel size of 2 μm. A high-speed Phantom V2010 camera (Vision Research Inc., Wayne, NJ, USA) recorded images at 10 000 frames per second for characterizing equilibrium orbits and 30 frames per second for analyzing long term behavior of particle motion inside the cavity. An in-house image processing code was developed in MATLAB to identify sizes of trapped particles and track particle motion in the cavity. Scatter plots were generated from 10–30 repeated runs in the same cavity and under flow conditions (Re). The fluorescence images were captured by a CCD Coolsnap HQ2 camera (Roper Scientific, Evry, France), then processed by Zen2 software. Cells that are not intact and cell fragments (a < 4 μm) were excluded from the study.

2.4 Particle and cell suspension

Fluorescent polystyrene particles with mean diameters of 10, 15, 20 and 30 μm were purchased from (Phosphorex, Hopkinton, MA). To prevent aggregation, 0.1% Tween 20

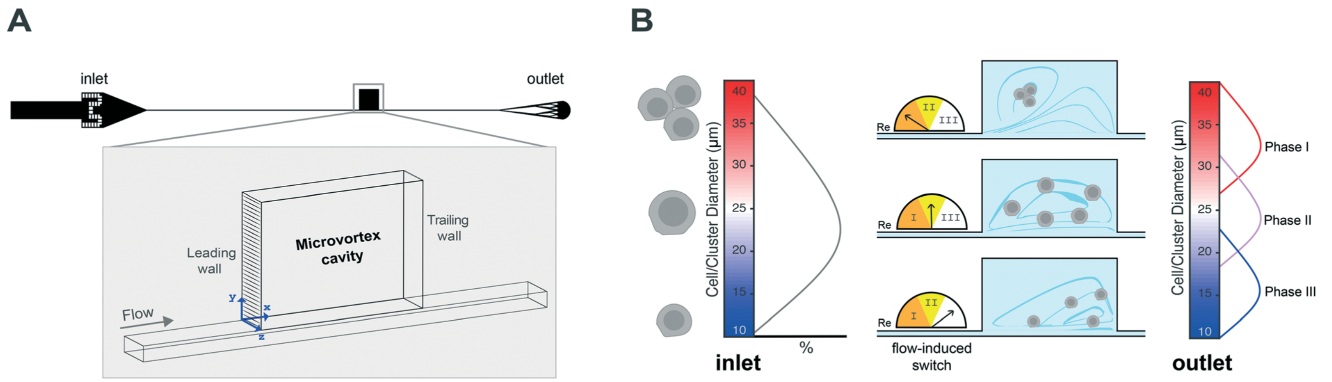

Fig. 1 Mircofluidic device principle and operation. (A) Schematic of a single channel device with a micro-cavity placed 1 cm from the inlet. Microvortex flow forms between the leading and trailing walls of the cavity at high Reynolds number. (B) Polydisperse rare cells (clusters and large and small cells) are captured by different microvortices generated in the same device. Inertial flow conditions (Re) are tuned to generate distinct vortical flow geometries with specific capturing properties: phase I (Re = 100–175) captures clusters, phase II (Re = 175–225) captures large cells and phase III (Re= 225–300) captures small cells.

(Sigma-Aldrich, product No. P9416) was added to the particle suspension. MCF-7 (30 2004, ATCC, Manassas, VA) and MDA-MB-231 (ATCC 30-2002) were cultured in DMEM medium (ATCC 30-2002). The medium was supplemented with 10% fetal bovine serum (Invitrogen, Carlsbad, CA) and 1% penicillin streptomycin (Invitrogen, Carlsbad, CA) at 37 °C under 5% CO_2 conditions. Cells were passaged once they reached an 80% confluence. The cells and medium tested negative for mycoplasma. We chose the MDA-MB-231 breast cancer cell line to model the rare cell capture. It is one of the most challenging model among cancer cell lines to capture due to the cells' heterogeneous receptor expression. More importantly, they are relatively smaller than other cancer cells in addition to their size overlap with WBCs. Cells were stained with final concentrations of 0.005 mg ml^{-1} DAPI (40,6-diamidino-2-phenylindole, Molecular Probes) and 0.05 mg ml^{-1} anti-CD45-PE (BD Biosciences, HI30) in blood spiking experiments. MDA-MB-231 GFP expressing cells, which we will refer to as MDA-GFP, were spiked in diluted blood with PBS by a factor of 20×. Stained cells were defined in Fig. S5a.† Captured cells in the microvortex flow were released from the device and collected in a well plate for counting and cell size distribution analysis. Media were added into the well plate and the cells were incubated under the same growth conditions for viability tests. Previous studies provide a detailed description of the collection method for captured cells and viability tests.[40–42] Whole blood samples from three different healthy donors, with informed consents, were obtained in EDTA venous blood collection tubes (Vacutainer, BD Biosciences, San Jose, CA). The protocol was reviewed and approved by the UCLA IRB (UCLA-IRB#11-001120).

2.5 Simulation

We modeled the device using COMSOL Multiphysics (COMSOL, Burlington, MA) to quantify the stabilized streamlines and velocity distribution of the microvortex flow. The flow rate was set from 100–1000 μL min^{-1}. Water was applied as a carrier fluid in the simulation with the following physical properties (density ρ = 1000 kg m^{-3} and dynamic viscosity $\mu = 10^{-3}$ kg m^{-1} s^{-1}). The velocity magnitude (m s^{-1}) is calculated from the flow rate applied in the inlet velocity. The plotted range of velocity magnitude saturates at 0.04 m s^{-1} to show the vortex core of each microvortex flow (Fig. S2a†). The vortex core coordinates x_0 and y_0 are used as the reference point of the system and particle motion with time (t) (Fig. S2b†). The vortex core coordinates are set to the local velocity minimum within the cavity boundaries' x–y cross-sections along the x-axis. (Fig. S2c†). There was a small shift in the vortex core coordinates between simulations and the experimental study due to PDMS deformation.

3 Results and discussion

3.1 Particle migration to microvortex flow

Before describing particle motion and separation in the cavity, we explain the important parameters that influence particle transition from the main channel to the open cavity. The inertial flow is described in terms of the Reynolds number ($\mathrm{Re} = \rho U D_h/\mu$), which is controlled by varying the flow rate Q (μL min^{-1}). Here ρ, U and μ correspond to the density, average inlet velocity and dynamic viscosity of the fluid, respectively. D_h is the hydraulic diameter of the channel, defined as ($D_h = 2(W_{ch}H_{ch})/(W_{ch}H_{ch})$), where H_{ch} and W_{ch} are the channel height and width respectively. At finite Reynolds number, suspended particles under bounded conditions experience two counteracting forces.[49] In Newtonian fluids, these forces control the particle's lateral migration in the channel. Shear gradient lift force (F_{LS}) pushes the particle towards the channel wall, while wall induced lift force (F_{LW}) directs the particle towards the channel centerline. Particles migrate towards an equilibrium position.[30,31,50] The inertial lift forces are simplified as the following, ($F_{LS} = f_L\rho U^2a^3/\mathrm{W}_{ch}$) and ($F_{LW} = f_L\rho U^2a^6/W_{ch}{}^4$), where f_L is the dimensionless lift coefficient and a is the particle diameter.

Particles experience different magnitudes of hydrodynamic forces based on their size. Particle sizes were scaled in relation to the channel width (W_{ch}) to define a blockage ratio ($\lambda = a/W_{ch}$). The channel was designed such that all tested particles, cells and cell clusters reach equilibrium positions before passing through the cavity. The channel aspect ratio ($\mathrm{AR} = H_{ch}/W_{ch}$) is 1.75 to align particles laterally in the mid-section of each wall.[51,52]

The vortical flow inside the cavity is strongly influenced by the characteristics of the main channel flow (Re). At low Reynolds number ($\mathrm{Re} < 10$), the fluid flow passes with fore-aft symmetry through the cavity with no recirculation (Fig. S2a†).[53] Moffat eddies are formed in the leading wall corners at slightly higher flow rates,[54] where particles pass through the cavity with no entrapment. However, as the inertial conditions ramp ($\mathrm{Re} \sim 70$), the flow separates from the main channel and forms a jet effect in the channel expansion region. Microvortex formation has been described extensively in previous studies.[35,37] In the sudden expansion–contraction region, particles are driven into the cavity due to the absence of wall induced lift force (F_{LW}) and other fluid dynamic effects.[47] Some particles are stable in the recirculating fluid flow, however not all are retained in the cavity (*i.e.* short residence time) depending on their size (λ).

3.2 Microvortex size-based radial separation

In this section, we explore the long term behavior of neutrally buoyant particles inside a microvortex flow after entrapment. Under the same flow conditions in microvortex flows, the particles settle in separate equilibrium orbits based on their size. Upon changing the flow rate, the equilibrium orbits change their radius. We tracked the motion of polystyrene beads in the cavity under different flow conditions. Each flow rate forms a unique vortex topology with size-specific capturing properties.

To systemically understand the size-based orbits and their migration, we transform the particle motion from Cartesian

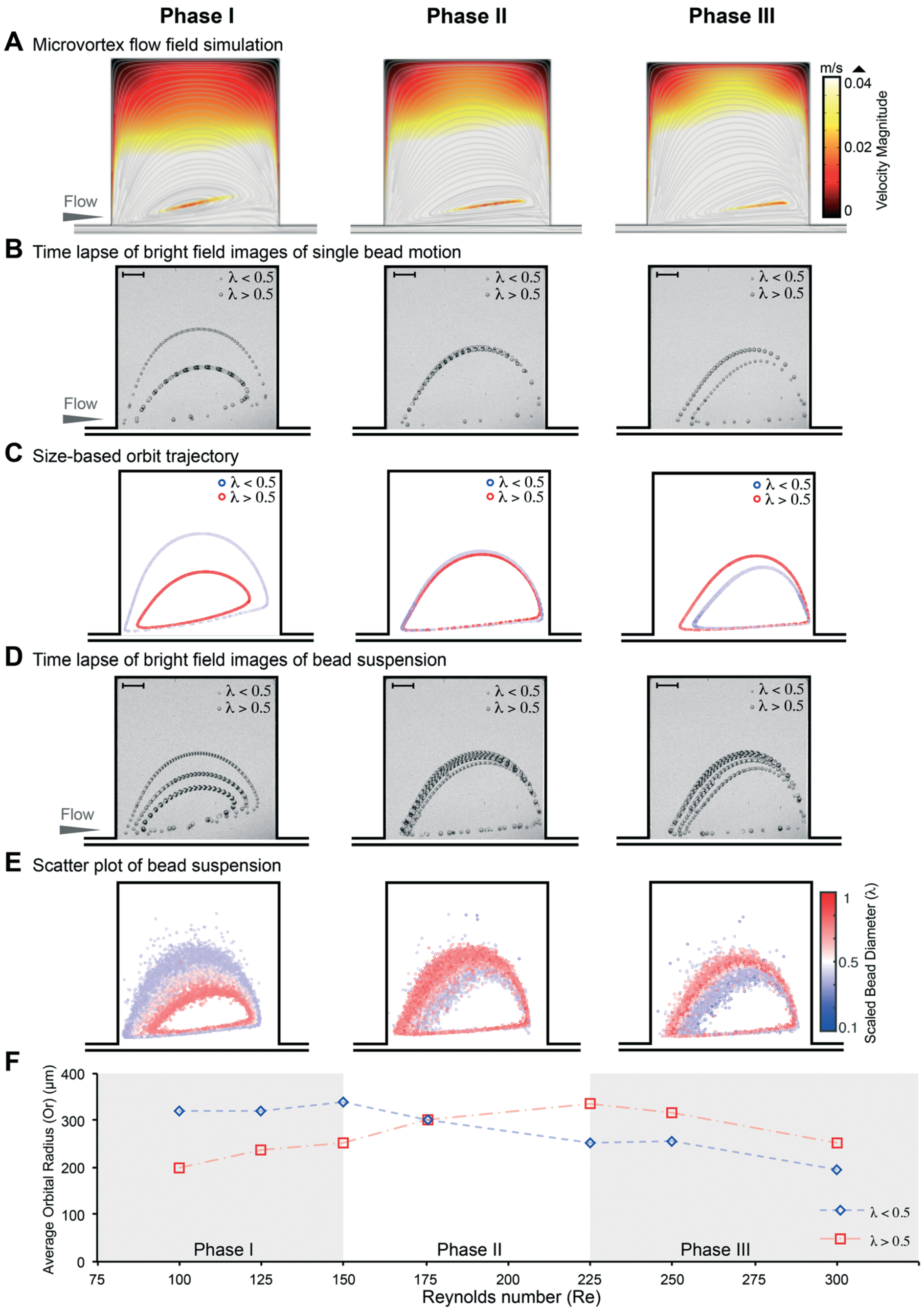

Fig. 2 Radial migration under different inertial flow conditions (Re): the three columns of images (A–E) represent an example of the inertial flow conditions in phase I (Re = 100–175), phase II (Re= 175–225) and phase III (Re = 225–300). (A) Flow field simulation shows flow streamlines (grey lines) and velocity distribution (color contours) of the laminar vortical flow in the cavity with an aspect ratio (AR) = 1 at Re = 150, 200 and 300. The color scale represents the velocity magnitude (m s^{-1}). (B) High-speed time-lapse images of single polystyrene beads show the transition of size-based equilibrium orbits in each capture phase. (C) Bead trajectories show inward radial migration inversion between large ($\lambda > 0.5$) (red) and small beads ($\lambda < 0.5$) (blue) after phase II. (D) High-speed time-lapse images of polystyrene bead suspensions illustrate the transition between phases. All scale bars represent 120 μm. (E) Scatter plots of polydisperse polystyrene beads illustrate orbital transition towards the vortex core between phase I and phase III. The color scale represents scaled bead diameter (λ). (F) Average orbital radius (O_r) of polydisperse beads in different Re illustrates the switching of the size-dependent orbit in a stable capture region towards the vortex core.

coordinates to polar coordinates. Two-dimensional particle trajectories $[x_p(t), y_p(t)]$ were translated to an average orbital radius (O_r) describing the net particle behavior in micro-vortex flows:

$$O_r = \sqrt{\left[x_p(t) - x_0\right]^2 + \left[y_p(t) - y_0\right]^2} \qquad (1)$$

We segment beads and cells into different sizes according to their blockage ratio (λ) and calculate their average orbital radius in the cavity at different flow rates. Under low inertial conditions, large particles ($\lambda > 0.5$) settle in small equilibrium orbits near the vortex core. However, small particles ($\lambda \leq 0.5$) orbit around the vortex boundary farther away from the vortex core. Upon increasing the flow rate, small and large particles switch their proximity to the vortex core (Video S1†). We describe the progression of this phenomenon and transition in the phases (Fig. 2). Each phase shows a size-based average orbital radius (O_r) change correlated with a range of inertial flow conditions defined by the Reynolds number.

3.2.1 Phase I. In this regime, the vortical microflow begins to be generated ($100 \leq \mathrm{Re} < 175$) and the vortex core is formed near the leading wall and then shifts to the middle of the cavity (Fig. 2A). Large particles spiral inward migrating toward the vortex core, leading to a decrease in their orbital radius. However, small beads settle in orbits away from the vortex core and near the cavity walls with a larger orbital radius $[O_{r_{(\lambda<0.5)}} > O_{r_{(\lambda>0.5)}}]$ (Fig. 2B). Particles with a large orbital radius are more unstable and can exit the cavity over time or through small flow fluctuations.

3.2.2 Phase II. Increasing the flow further to higher Reynolds numbers ($175 \leq \mathrm{Re} < 225$), the vortex core takes over the cavity pushing both large and small beads outward. In this case, large and small beads share the same orbit trajectory away from the vortex core and near the vortex boundary $[O_{r_{(\lambda<0.5)}} \simeq O_{r_{(\lambda>0.5)}}]$. Particle loading and accumulation in the cavity is limited due to a reduced number of trapping orbits. Large particles dominate the trapping space in this phase.

3.2.3 Phase III. Interestingly, at higher Reynolds numbers ($225 \leq \mathrm{Re} < 300$), an inversion occurs. Small beads begin to orbit near the vortex core while large beads migrate outward near the cavity walls $[O_{r_{(\lambda<0.5)}} < O_{r_{(\lambda>0.5)}}]$. The vortex core shifts from the center of the cavity to the trailing wall.

To further investigate radial separation in the cavity, we experimentally studied the trapping dynamics of polydisperse solutions of particles. Equal fractions of 10, 15, 20 and 30 μm polystyrene bead suspensions were passed through the cavity in all trapping phases (Fig. 2D). The scatter plot of the particle size distribution in the cavity and average orbital radius agrees with the observations in single particle trajectory analysis (Fig. 2E) (Video S2†). The average orbital radius (O_r) plot of the polydisperse beads shows switching in the equilibrium orbit proximity to the vortex core after phase II (Fig. 2F).

3.3 Tunable size selective capture of cells

Cells exhibit the same size-based radial migration as beads. In addition, we observed the same pattern of cell radial migration as a function of cavity aspect ratio (AR = 1, 2, 3) (Video S3†). We tested the size-selective capture properties of MDA-MB-231 breast cancer cells under different microvortex flow conditions (Fig. 3A–C). At the early stages of phase I, cell clusters $\lambda \geq 1$ are stably trapped in the vortex core with $O_r \approx 0$. Large cells dominate trapping orbits in phase II. Lastly, in phase III, small cells self-assemble in orbits near the vortex core and large cells settle near the vortex boundary (Fig. 3B). The scatter plots of cell size distribution over multiple experiments are shown for the three phases and AR = 2 (Fig. 3C). The same radial separation of beads for AR = 1 is observed (Fig. S3 and video S4†). Moreover, the average orbital radius (O_r) of cells with AR = 1 matches the bead results over all three phases (Fig. 3D). This implies that deformability differences do not play a significant role in the size-dependent inversion of orbital radius.

We investigated the relationship between inward radial migration with the size distribution of captured cells and the efficiency of capture (Fig. 3E). The mean cell-size of captured cells is significantly shifted when the orbital radius becomes smaller. Each vortex flow condition possesses a different capture distribution of cells. The total number of captured cells per cavity agrees with the results from a previous study.[40] The microvortex flow at Re = 150 has the highest number of captured cells but a low size specificity.

To investigate further, we compared the capture capacity of two different breast cancer cell lines with different size distributions (MCF-7 and MDA-MB-231). We found the optimal capture phase for each cell line: phase I for the larger MCF-7 and phase III for the smaller MDA-MB-231 (Fig. S4†). This result demonstrates the device tunability to enhance the capture of cells with different size distributions.

3.4 Rare cell capture in blood

From our findings, we defined the critical Reynolds numbers above which cells of a certain diameter occupy stable orbits towards the vortex core. Here, we tested the trapping ability to extend to a larger range of sizes for MDA-GFP cells from blood in a single device. Cells in diluted blood captured in the microvortex flow show stable orbit trajectories similar in shape to that of cells in buffer across all three capture phases (Fig. S5†). We spiked 1000 MDA-GFP cells in blood samples where we flowed them under optimal conditions for trapping small cells ($\lambda < 0.5$) in phase III (Re = 275) and large cells and clusters ($\lambda > 0.5$) in phase I (Re = 125). The sample was passed and recycled three times under phase I flow conditions and three times later under phase III flow conditions (Fig. 4A) and *vice versa* (Fig. 4B). Each trapping cycle showed a consistent size-selective capture. In addition, recycling the sample improved the capture efficiency. Captured cells were released on demand by stopping the inlet flow for enumeration and size distribution measurements. We found the same bias in captured cell size distribution in each phase independent of the order of processing (Fig. 4C). The size distribution of cells collected in the outlet show statistically significant differences of target cell mean size between phase I (Re = 125) and phase III (Re = 275) (p-value < 0.0001; $\alpha = 0.01$). We were able to obtain spiked cells under both flow conditions while maintaining scalable unit efficiency, high purity and cell viability (Fig. S6†).

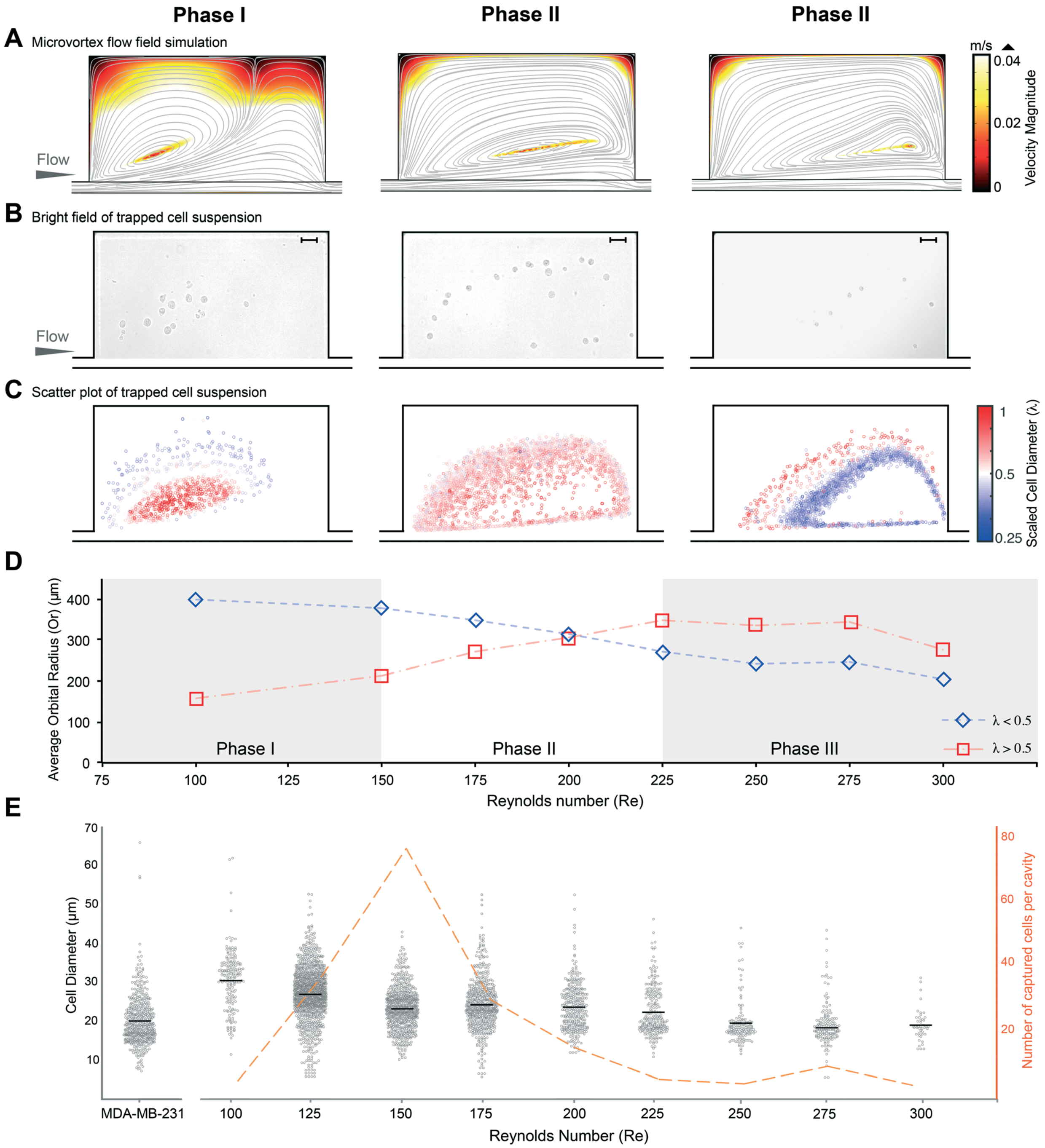

Fig. 3 Observed relationship between the size-dependent stable limit cycle orbit and size-based vortex capture of cells. The three columns of images (A–C) represent an example of the inertial flow conditions in phase I (Re = 100–175), phase II (Re = 175–225) and phase III (Re = 225–300). (A) Flow streamlines (grey lines) and velocity distribution (color contours) of laminar vortical flows in a cavity with an aspect ratio (AR) = 2 at Re = 100, 200, 300. The color scale represents the velocity magnitude (m s^{-1}). (B) MDA-MB-231 cells self-assemble in different size-dependent orbits. Phase I provides stable capture of cell clusters, phase II sustains large cells and phase III captures small cells. All scale bars represent 60 μm. (C) Size-labeled scatter plot of tracked cells inside the microvortex flow. The color scale represents scaled cell diameter (λ). (D) Average orbital radius (O_r) of polydisperse cells under different inertial conditions (Re) shows the switching in size-based equilibrium orbits after phase II. (E) Size distribution of captured cells at different Reynolds numbers (Re). The number of captured cells in one cavity (right secondary axis) illustrates the specific capture capacity of the microvortex flow at different Reynolds numbers (Re).

We next evaluated the ability to apply the two size-selective phases of capture for higher efficiency and throughput in sequential and parallel vortex trapping devices. We tested the previously demonstrated Vortex HT device under both phase I and phase III conditions. The capture efficiency for the smaller cell population of MDA-GFP cells was enhanced from close to 0 in phase I to 5% when operating in phase III. Combining operation in phase I and

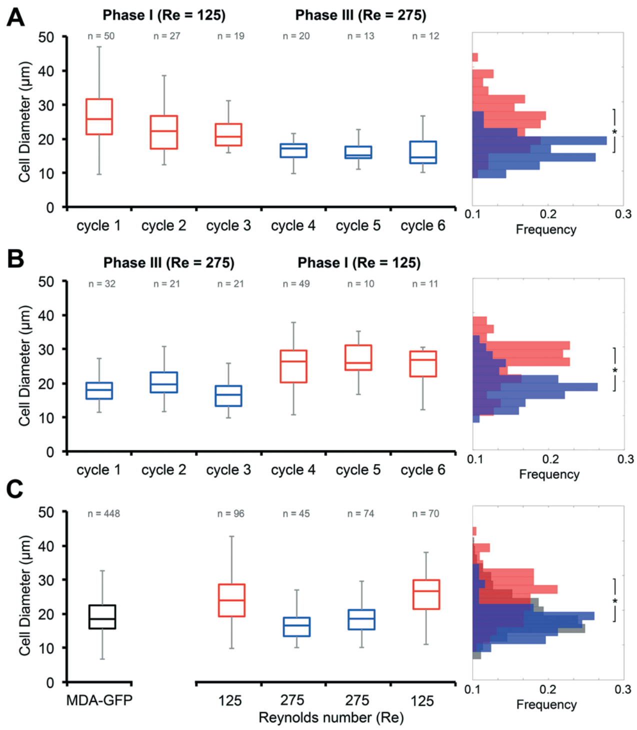

Fig. 4 Size-based capture of rare cells from blood. (A) Box-plot graph of isolated MDA-GFP size distribution from blood starting under phase I (Re = 125) flow conditions, followed by phase III (Re = 275). The blood sample was recycled in the device for each phase. The accumulated size distribution histogram is shown for captured cells from phase I (red) and phase III (blue) capture. (B) Box-plot graph of isolated MDA-GFP cells starting at phase III (Re = 275) followed by phase I (Re = 125) shows the same trend in size-selective capture. (C) Captured cells for each phase no matter what the order is shows significant differences in the cell size distribution. By processing over phase I (Re = 125) (red) and phase III (Re = 275) (blue) we can extend the capture of MDA-MB-231 cells with a size distribution (grey). (*) *p*-value < 0.0001.

phase III in the Vortex HT device led to a total efficiency of ~24% (Fig. S7†).

4 Conclusion

In this work, we report a membrane-less filter with flow rate tunable selectivity of particle size. It enables long-term trapping of rare cells from complex suspensions in a confined cavity flow. A flow-dependent switch in the vortical flow morphology modulated the size-based trapping properties. A wide distribution of cell sizes is captured by tuning the flow rate in a single device, including single cells and cell clusters in the same cavity geometry. In addition, it facilitates on-chip testing and analysis of polydisperse cells. This method is scalable by increasing the number of capturing units. Ultimately, this one-device-fits-all-sizes system opens new opportunities for sampling and separation of an expanded range of target particles from complex suspensions. Finally, we anticipate that the presented technology is universal for on-chip particle profiling and characterization for industrial and biomedical applications.

Acknowledgements

The authors thank Dr. Oladunni Adeyiga for her contribution in blood sample collection. We gratefully acknowledge the support of the California NanoSystems Institute (CNSI) at the University of California, Los Angeles.

References

1 Y. Chen, P. Li, P.-H. Huang, Y. Xie, J. D. Mai, L. Wang, N.-T. Nguyen and T. J. Huang, *Lab Chip*, 2014, **14**, 626–645.
2 W. Lee, P. Tseng and D. Di Carlo, in *Microtechnology for Cell Manipulation and Sorting*, Springer, 2017, pp. 1–14.
3 K.-H. Han and A. B. Frazier, *Lab Chip*, 2008, **8**, 1079–1086.
4 B. Çetin and D. Li, *Electrophoresis*, 2011, **32**, 2410–2427.
5 V. Gupta, I. Jafferji, M. Garza, V. O. Melnikova, D. K. Hasegawa, R. Pethig and D. W. Davis, *Biomicrofluidics*, 2012, **6**, 024133.
6 T. P. Forbes and S. P. Forry, *Lab Chip*, 2012, **12**, 1471–1479.
7 K.-H. Han and A. B. Frazier, *Lab Chip*, 2006, **6**, 265–273.
8 N. Xia, T. P. Hunt, B. T. Mayers, E. Alsberg, G. M. Whitesides, R. M. Westervelt and D. E. Ingber, *Biomed. Microdevices*, 2006, **8**, 299–308.
9 M. Hejazian, W. Li and N.-T. Nguyen, *Lab Chip*, 2015, **15**, 959–970.
10 Z. Wang and J. Zhe, *Lab Chip*, 2011, **11**, 1280–1285.
11 A. H. Yang and H. T. Soh, *Anal. Chem.*, 2012, **84**, 10756–10762.
12 F. Petersson, L. Åberg, A.-M. Swärd-Nilsson and T. Laurell, *Anal. Chem.*, 2007, **79**, 5117–5123.
13 J. Nam, H. Lim, D. Kim and S. Shin, *Lab Chip*, 2011, **11**, 3361–3364.
14 F. Petersson, A. Nilsson, C. Holm, H. Jönsson and T. Laurell, *Analyst*, 2004, **129**, 938–943.
15 D. G. Grier, *Nature*, 2003, **424**, 810–816.
16 J. Cheng, M. A. Rahman and A. T. Ohta, in *Microtechnology for Cell Manipulation and Sorting*, Springer, 2017, pp. 93–128.
17 D. R. Gossett, W. M. Weaver, A. J. Mach, S. C. Hur, H. T. K. Tse, W. Lee, H. Amini and D. Di Carlo, *Anal. Bioanal. Chem.*, 2010, **397**, 3249–3267.
18 M. Yamada, M. Nakashima and M. Seki, *Anal. Chem.*, 2004, **76**, 5465–5471.
19 J. Takagi, M. Yamada, M. Yasuda and M. Seki, *Lab Chip*, 2005, **5**, 778–784.
20 M. Pødenphant, N. Ashley, K. Koprowska, K. U. Mir, M. Zalkovskij, B. Bilenberg, W. Bodmer, A. Kristensen and R. Marie, *Lab Chip*, 2015, **15**, 4598–4606.
21 L. R. Huang, E. C. Cox, R. H. Austin and J. C. Sturm, *Science*, 2004, **304**, 987–990.
22 D. L. Adams, R. K. Alpaugh, S. S. Martin, M. Charpentier, S. Chumsri, M. Cristofanilli, D. K. Adams, O. V. Makarova, P. Zhu and S. Li, *et al.*, *RSC Adv.*, 2016, **6**, 6405–6414.
23 M. Yamada, W. Seko, T. Yanai, K. Ninomiya and M. Seki, *Lab Chip*, 2017, **17**, 304–314.
24 S. C. Hur, N. K. Henderson-MacLennan, E. R. McCabe and D. Di Carlo, *Lab Chip*, 2011, **11**, 912–920.

25 D. R. Gossett, H. T. K. Tse, J. S. Dudani, K. Goda, T. A. Woods, S. W. Graves and D. Di Carlo, *Small*, 2012, **8**, 2757–2764.

26 M. E. Warkiani, B. L. Khoo, L. Wu, A. K. P. Tay, A. A. S. Bhagat, J. Han and C. T. Lim, *Nat. Protoc.*, 2016, **11**, 134–148.

27 X. Wang and I. Papautsky, *Lab Chip*, 2015, **15**, 1350–1359.

28 J. Zhang, W. Li and G. Alici, in *Advanced Mechatronics and MEMS Devices II*, Springer, 2017, pp. 563–593.

29 J. Zhang, S. Yan, D. Yuan, G. Alici, N.-T. Nguyen, M. E. Warkiani and W. Li, *Lab Chip*, 2016, **16**, 10–34.

30 D. Di Carlo, *Lab Chip*, 2009, **9**, 3038–3046.

31 D. Di Carlo, J. F. Edd, K. J. Humphry, H. A. Stone and M. Toner, *Phys. Rev. Lett.*, 2009, **102**, 094503.

32 H. Amini, E. Sollier, W. M. Weaver and D. Di Carlo, *Proc. Natl. Acad. Sci. U. S. A.*, 2012, **109**, 11593–11598.

33 J. M. Martel and M. Toner, *Annu. Rev. Biomed. Eng.*, 2014, **16**, 371.

34 C. Alix-Panabières and K. Pantel, *Nat. Rev. Cancer*, 2014, **14**, 623–631.

35 S. C. Hur, A. J. Mach and D. Di Carlo, *Biomicrofluidics*, 2011, **5**, 022206.

36 J. Che, A. J. Mach, D. E. Go, I. Talati, Y. Ying, J. Rao, R. P. Kulkarni and D. Di Carlo, *PLoS One*, 2013, **8**, e78194.

37 A. J. Mach, J. H. Kim, A. Arshi, S. C. Hur and D. Di Carlo, *Lab Chip*, 2011, **11**, 2827–2834.

38 D. A. Vickers, M. Ouyang, C. H. Choi and S. C. Hur, *Anal. Chem.*, 2014, **86**, 10099–10105.

39 J. Che, V. Yu, E. B. Garon, J. W. Goldman and D. Di Carlo, *Lab Chip*, 2017, **17**, 1452–1461.

40 E. Sollier, D. E. Go, J. Che, D. R. Gossett, S. O'Byrne, W. M. Weaver, N. Kummer, M. Rettig, J. Goldman and N. Nickols, *et al.*, *Lab Chip*, 2014, **14**, 63–77.

41 M. Dhar, J. Wong, A. Karimi, J. Che, C. Renier, M. Matsumoto, M. Triboulet, E. B. Garon, J. W. Goldman and M. B. Rettig, *et al.*, *Biomicrofluidics*, 2015, **9**, 064116.

42 J. Che, V. Yu, M. Dhar, C. Renier, M. Matsumoto, K. Heirich, E. B. Garon, J. Goldman, J. Rao and G. W. Sledge, *et al.*, *Oncotarget*, 2016, **7**, 12748–12760.

43 D. Vigolo, S. Radl and H. A. Stone, *Proc. Natl. Acad. Sci. U. S. A.*, 2014, **111**, 4770–4775.

44 T. Karino and H. Goldsmith, *Philos. Trans. R. Soc., B*, 1977, **279**, 413–445.

45 T. Karino and H. Goldsmith, *Microvasc. Res.*, 1979, **17**, 217–237.

46 J. Zhou, S. Kasper and I. Papautsky, *Microfluid. Nanofluid.*, 2013, **15**, 611–623.

47 H. Haddadi and D. Di Carlo, *J. Fluid Mech.*, 2017, **811**, 436–467.

48 C. Renier, E. Pao, J. Che, H. E. Liu, C. A. Lemaire, M. Matsumoto, M. Triboulet, S. Srivinas, S. S. Jeffrey and M. Rettig, *et al.*, *Nature Precision Oncology*, 2017, **1**, 15.

49 G. Segre, *Nature*, 1961, **189**, 209–210.

50 D. Di Carlo, D. Irimia, R. G. Tompkins and M. Toner, *Proc. Natl. Acad. Sci. U. S. A.*, 2007, **104**, 18892–18897.

51 C. Liu, C. Xue, J. Sun and G. Hu, *Lab Chip*, 2016, **16**, 884–892.

52 K. Hood, S. Kahkeshani, D. Di Carlo and M. Roper, *Lab Chip*, 2016, **16**, 2840–2850.

53 Z. Wu, Y. Chen, M. Wang and A. J. Chung, *Lab Chip*, 2016, **16**, 532–542.

54 H. Moffatt, *J. Fluid Mech.*, 1964, **18**, 1–18.